

## Electronic Supplementary Information (ESI): Stress and stretching regulate dispersion in viscoelastic porous media flows

Manish Kumar,<sup>1,\*</sup> Derek M. Walkama,<sup>2,3,\*</sup> Arezoo M. Ardekani,<sup>1</sup> and Jeffrey S. Guasto<sup>2,‡</sup>

<sup>1</sup>*Department of Mechanical Engineering, Purdue University,  
585 Purdue Mall, West Lafayette, Indiana 47907, USA*

<sup>2</sup>*Department of Mechanical Engineering, Tufts University,  
200 College Avenue, Medford, Massachusetts 02155, USA*

<sup>3</sup>*Department of Physics and Astronomy, Tufts University,  
574 Boston Avenue, Medford, Massachusetts 02155, USA*

### I. ORDERED AND DISORDERED MICROFLUIDIC POROUS MEDIA

Microfluidic porous media devices were designed with precisely the same geometry as Walkama *et al.* [1] and have a 25 mm long, 4 mm wide, and 50  $\mu\text{m}$  high main channel. The microfluidic channels contain arrays of cylindrical pillars (diameter,  $d = 50 \mu\text{m}$ ) arranged in either an ordered hexagonal lattice with a staggered orientation relative to the flow [2] or a disordered array (Fig. S1). Photolithography masks were generated by first specifying an ordered, hexagonal array of pillar locations with a lattice constant,  $a = 120 \mu\text{m}$ . Disorder arrangements were created by perturbing each pillar from their original location. New pillar locations were sampled from a random uniform distribution within a hexagon (Fig. S1) of circumradius,  $\beta a$ , where  $\beta$  is a fraction of the lattice constant in the range  $0 \leq \beta \leq 1$ . Two different geometries were investigated including an ordered hexagonal array corresponding to  $\beta = 0$  and a disordered arrangement with  $\beta = 1$ .

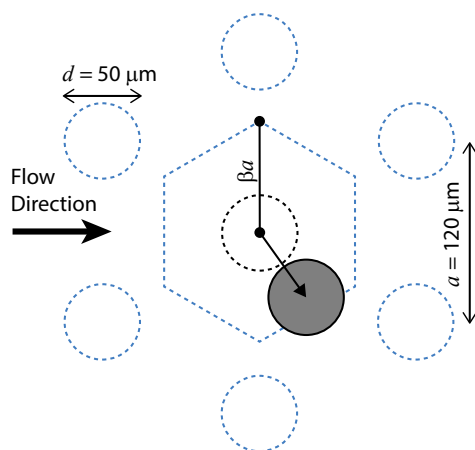


FIG. S1. Diagram of the ordered geometry (dashed circles) based on a hexagonal lattice having a staggered orientation relative to the flow direction. The disordered geometry is generated by perturbing the ordered geometry within a circumradius (dashed hexagon),  $\beta a$ , of the original lattice point.

### II. RHEOLOGY OF VISCOELASTIC POLYMER SOLUTIONS

Capillary breakup extensional rheology (CaBER) [3] was used to extract the relaxation time of the viscoelastic PAA and glycerol solutions (see Methods in main text). A droplet of the viscoelastic fluid was stretched rapidly between the ends of two circular cylinders, and the capillary bridge diameter,  $D(t)$ , was measured as a function of time,  $t$ , with a laser micrometer [Fig. S2(a)]. The capillary bridge diameter decays exponentially at early times with

\* These authors contributed equally.

‡ Corresponding author: Jeffrey.Guasto@tufts.edu

a decay constant  $3\tau$  [4]. A single trial represents a separate loading of the viscoelastic PAA fluid in the CaBER rheometer, which was tested four times each and averaged to obtain the bridge diameter curves shown. The slope of this exponential regime [Fig. S2(a), shaded area] was fitted and averaged over several trials ( $N = 6$ ) to determine a relaxation time of  $\tau = 1.14 \pm 0.1$  s. This measured relaxation time for the fluid used in our experiments is well within the range of relaxation times for similar compositions of PAA and glycerol solutions reported in the literature (0.1-10 s) [5–7].

The shear viscosity,  $\eta$ , of the viscoelastic solution was measured at various shear rates using a strain controlled rheometer (TA-2000) with a cone and plate geometry [Fig. S2(b)]. The polymer solution was pre-sheared at a rate of  $1 \text{ s}^{-1}$  for 120 s, then each measurement was held at the respective shear rate for 60 s and measured for 15 s. This process was repeated for several trials ( $N = 5$ ) and averaged [Fig. S2(b)]. The shear response of the PAA solution was fitted by the Carreau-Yasuda model [8], where equation and fitting parameters are provided in Fig. S2(b). The solutions showed a weak shear thinning of the viscosity from 2 to 0.5 Pa·s between shear rates  $10^{-1}$  and  $10^2 \text{ s}^{-1}$ .

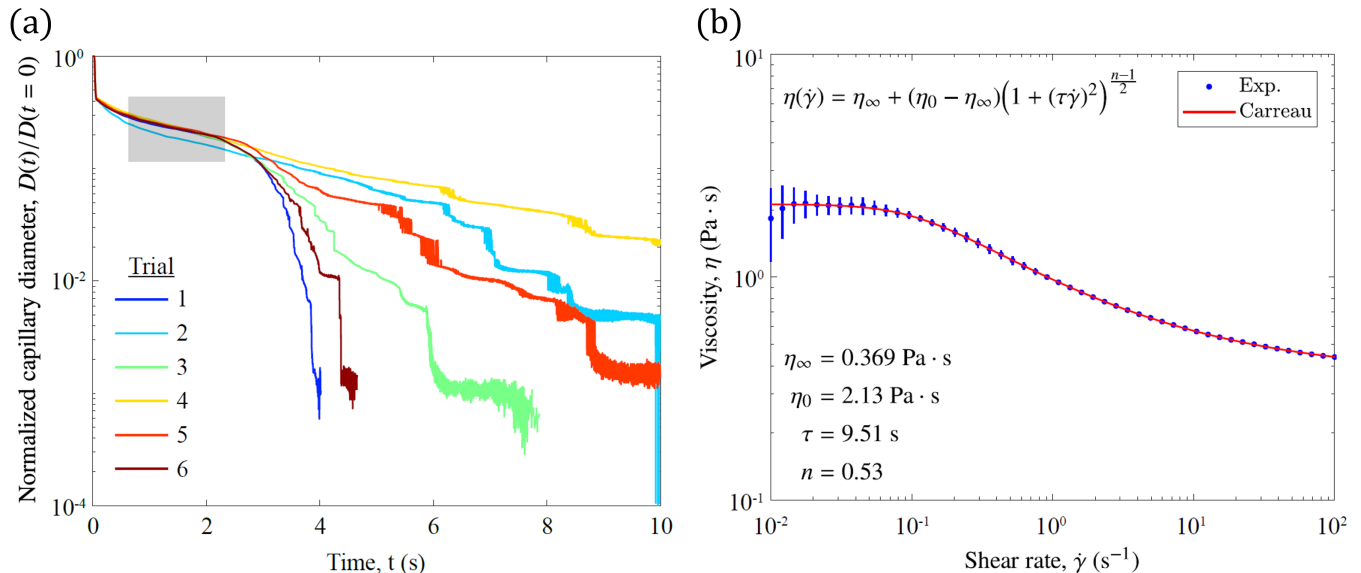


FIG. S2. Extensional and shear rheology of PAA solutions. (a) Capillary breakup extensional rheology (CaBER) measurement of viscoelastic PAA solutions showing the normalized capillary bridge diameter measured as a function of time for several independent trials ( $N = 6$ ). The capillary bridge diameter curves are fitted within the exponential regime (shaded area) to determine their slope and thus the relaxation time of the fluid. (b) Shear rheology reveals a weakly shear thinning behavior of the PAA solution viscosity within the range of typical shear rates of the porous media experiments. The points represent the mean, and the error bars indicate the standard deviation measured over several different sample loadings ( $N = 5$ ). The red curve is a Carreau-Yasuda model fit of the experimental data, and the equation and fitted parameters are shown.

### III. MESH AND TIME-STEP VALIDATION

The pressure drop ( $\Delta p$ ) across the porous geometry was used as a metric for mesh and time-step validation [9]. The pressure drops across the ordered porous geometry for different numerical meshes and the different values of the maximum Courant number are shown in Fig. S3. Along with the global mesh resolution of  $n_x \times n_y$ , the five layers close to each cylinder have been further refined. The Courant number (Co) controls the time-step size in the simulation, which has been defined as:

$$\text{Co} = \frac{\Delta t}{2V} \sum_{\text{faces}_i} |\phi_i|, \quad (\text{S1})$$

where  $\Delta t$ ,  $V$ , and  $\phi$  are the simulation time-step, cell volume, and the cell-face volumetric flux, respectively.  $\sum_{\text{faces}_i}$  shows the summation over all cell faces. The simulation becomes time-step independent for  $\text{Co}_{\text{max}} \leq 0.04$  and mesh independent for  $n_x \times n_y \geq 400 \times 400$  [Fig. S3(a)]. Therefore, we have used  $\text{Co}_{\text{max}} = 0.04$  and  $n_x \times n_y = 512 \times 512$  throughout the study. The convergence study at a large Wi ( $\text{Wi} = 3$ ) has been shown in Fig. S3(b). The pressure drop across the geometry at a large Wi fluctuates with time due to the chaotic flow in the ordered porous geometry

at a large  $Wi$ . However, the mean value of  $\Delta p$  is independent of mesh resolution, and hence the mesh resolution  $n_x \times n_y = 512 \times 512$  is sufficient for the mesh-independent results even at large  $Wi$ .

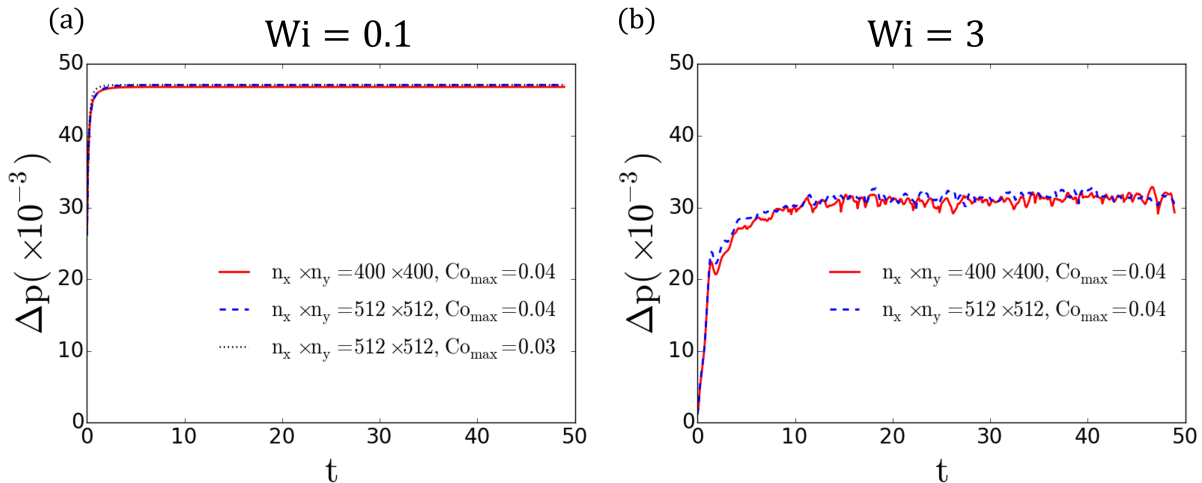


FIG. S3. Normalized pressure drop across the ordered porous geometry for (a) different mesh resolution and different maximum Courant number ( $Co_{\max}$ ) at a small  $Wi$  ( $Wi = 0.1$ ) and (b) different mesh resolution at a large  $Wi$  ( $Wi = 3$ ).

#### IV. EXPERIMENTALLY MEASURED DISPERSION TENSOR

Due to the anisotropic spreading of the tracer ensemble as well as the time-dependent nature of the dispersion that is detailed in the main text (Fig. 3 and corresponding text), we examine the time-dependent dispersion tensor [10, 11]:

$$D_{T,L}(\tilde{t}) = \int_0^{\tilde{t}} C_{T,L}(t') dt'. \quad (S2)$$

Here,  $C_{T,L}(\tilde{t})$  is the time-dependent velocity autocovariance detailed in Eqns. (10-11) in the main text, and  $\tilde{t} = tU/l$  is dimensionless time.  $U$  is the mean flow speed, and  $l = a \sin 60^\circ$  is the stream-wise pillar spacing. The experimentally measured dispersion tensor components in absolute units are shown in Fig. S4 as a function of dimensionless time. These results correspond to the normalized dispersion presented in the main text (Fig. 3).

#### V. PAKDEL–MCKINLEY PARAMETER FOR THE ORDERED POROUS GEOMETRY

The Pakdel–McKinley ( $M$ ) parameter provides a criterion for purely elastic instability in curved geometries [12] and is defined as:

$$M = \left[ \frac{\sigma_{11}}{\eta_0 \dot{\gamma}} \tau U \kappa \right]^{1/2}, \quad (S3)$$

where  $\sigma_{11}$  is the tensile stress along the streamline direction,  $\kappa$  is the streamline curvature and  $\dot{\gamma}$  is the magnitude of the shear rate. Local  $M$  fields in the ordered porous geometry simulations at different  $Wi$  are shown in Fig. S5. The maximum value of the  $M$  parameter ( $M_{\max}$ ) was observed to increase with  $Wi$ . Close to the onset of elastic instability, it is recognized that  $M_{\max}$  becomes greater than a critical value (i.e.,  $M_{\max} > M_{cr}$  as  $Wi \rightarrow Wi_{cr}$ ) [13]. The location of  $M_{\max}$  is the most sensitive region for the elastic instability [9, 14]. Just before the elastic instability,  $M_{\max}$  occurs in the cross-stream side of the cylinder for an isolated cylinder. However, it occurs in the region between the cylinders for a pair of cylinders [9]. Due to the staggered arrangement of the cylinders in the ordered porous geometry, the cross-stream sides of each cylinder lie in the region between a streamwise pair of cylinders, which amplifies the value of  $M_{\max}$ . Therefore, the elastic instability in ordered porous geometry occurs at a smaller  $Wi$  compared to isolated cylinders [9, 15].

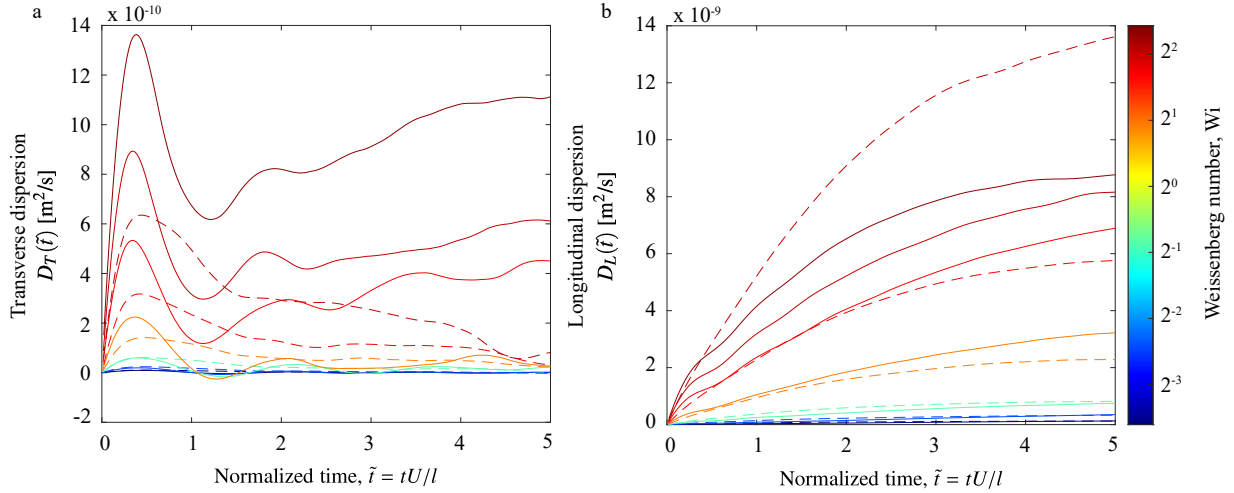


FIG. S4. Comparison of experimentally measured dispersion tensor components with absolute units in the (a) transverse and (b) longitudinal directions as a function of dimensionless time,  $\tilde{t}$ . Solid and dashed curves correspond to ordered and disordered media, and correspond to the non-dimensionalized version in Fig. 3 (main text). Weissenberg number,  $Wi$ , and  $\tilde{t}$  are based on flow speeds:  $U = [3.75, 8.05, 24.40, 82.38, 141.98, 177.65, 223.28] \mu\text{m/s}$  for ordered media and  $U = [3.66, 7.96, 19.20, 43.86, 91.83, 186.50] \mu\text{m/s}$  for disordered media.

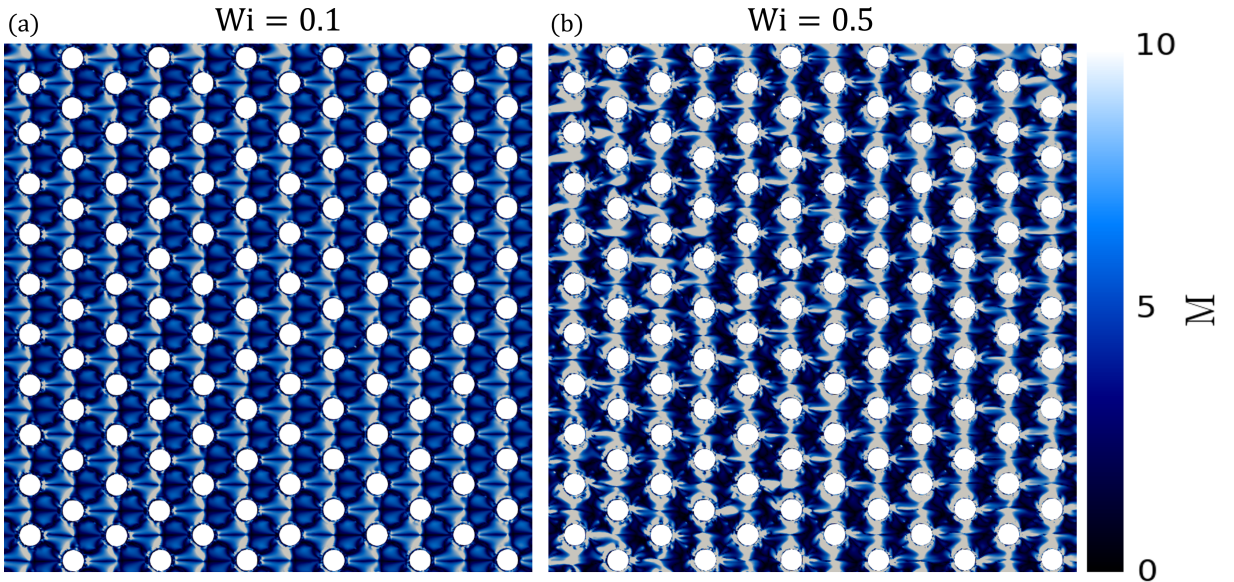


FIG. S5. The Pakdel-McKinley ( $M$ ) parameter in the ordered porous geometry simulations at (a)  $Wi = 0.1$  and (b)  $Wi = 0.5$ .

- 
- [1] D. M. Walkama, N. Waisbord, and J. S. Guasto, *Physical Review Letters* **124**, 164501 (2020).  
[2] S. J. Haward, C. C. Hopkins, and A. Q. Shen, *Proceedings of the National Academy of Sciences* **118**, e2111651118 (2021).  
[3] S. L. Anna and G. H. McKinley, *J. Rheol.* **45**, 115 (2001).  
[4] V. Entov and E. Hinch, *J. Nonnewton. Fluid Mech.* **72**, 31 (1997).  
[5] P. E. Arratia, C. C. Thomas, J. Diorio, and J. P. Gollub, *Phys. Rev. Lett.* **96**, 144502 (2006).  
[6] A. E. Koser, L. Pan, N. C. Keim, and P. E. Arratia, *Lab Chip* **13**, 1850 (2013).  
[7] B. Qin and P. E. Arratia, *Phys. Rev. Fluids* **2**, 083302 (2017).  
[8] R. Bird, R. Bird, R. Armstrong, and O. Hassager, *Dynamics of Polymeric Liquids, Volume 1: Fluid Mechanics*, Dynamics of Polymeric Liquids (Wiley, 1987).

- [9] M. Kumar and A. M. Ardekani, *Physics of Fluids* **33**, 074107 (2021).
- [10] R. S. Maier, D. M. Kroll, R. S. Bernard, S. E. Howington, J. F. Peters, and H. T. Davis, *Physics of Fluids* **12**, 2065 (2000).
- [11] F. Babayekhorasani, D. E. Dunstan, R. Krishnamoorti, and J. C. Conrad, *Soft Matter* **12**, 5676 (2016).
- [12] P. Pakdel and G. H. McKinley, *Phys. Rev. Lett.* **77**, 2459 (1996).
- [13] S. J. Haward, G. H. McKinley, and A. Q. Shen, *Sci. Rep.* **6**, 33029 (2016).
- [14] M. Kumar and A. M. Ardekani, *The European Physical Journal Special Topics* **123** (2022), 10.1140/epjs/s11734-022-00657-9.
- [15] M. Kumar and A. M. Ardekani, *Physical Review Fluids* **7**, 093302 (2022).